Chapter 3

Experimental methods and instrumentation

In this chapter, we first discuss the growth mechanism of ZnO nanostructures, which were grown using the thermal evaporation method. Then, the characterization that was performed will be discussed.

3.1. Thermal evaporation method

Of the various methods available for synthesizing nanostructures, thermal evaporation is one of the simplest techniques for growing oxide nanostructures. In addition, thermal evaporation provides a particularly cost effective and high quality equilibrium process, in which the morphology of nanostructures can be controlled by the content and melting points of the sources and substrates used. Thus, this process is frequently found in the literature, where researchers have presented the use of this model for growing semiconductors nanostructures. Thermal evaporation has proven to be very successful and versatile in the fabrication of NBs and NWs that have various characteristics. Photographs of our set-up, taken from different viewpoints, as well as temperature calibration of the horizontal furnace in this set-up, are shown in Fig. 3.1.

The basic process of this method is the sublimation of source material (solid phase; in powder form) at high temperature, a subsequent deposition of the vapor, which occurs in a certain temperature region, was carried out to form the desired nanostructures.

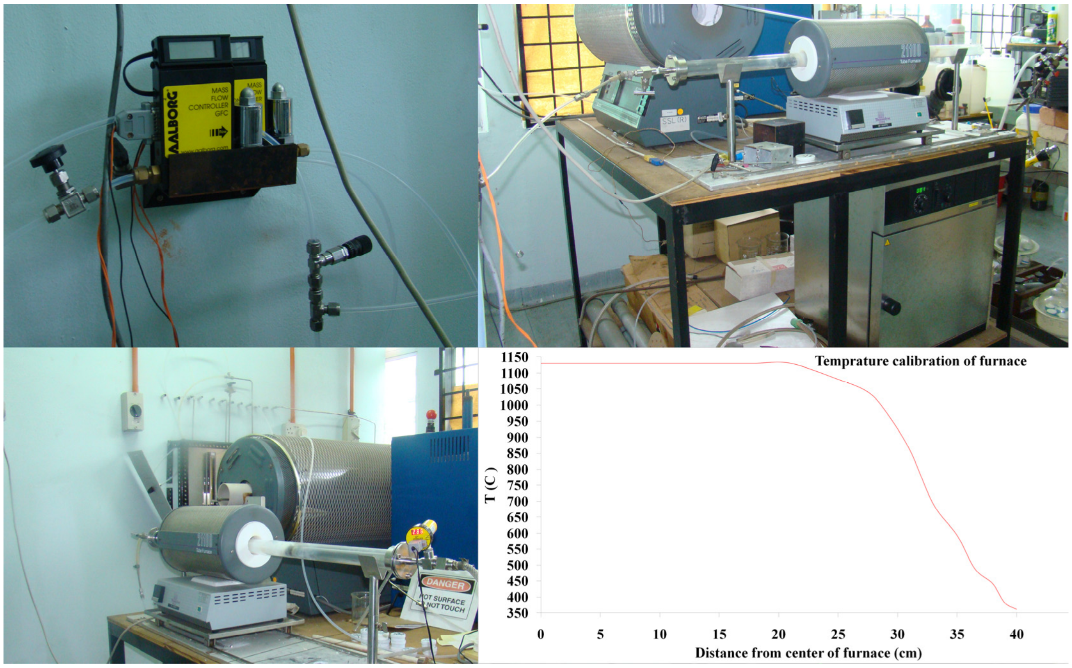

Figure 3.1. Photographs of the experimental set-up from different points-of-view, including the thermal evaporation system and two mass flow meters, which control gas flow during the experiment based on sccm (standard cubic centimeters per minute), as well as a temperature calibration diagram.

3.1.1. Conventional thermal evaporation set-up

A horizontal tube furnace that has a temperature gradient along its length, which decreases from the center of the furnace to the edge, is one of the simplest facilities for undertaking this deposition (Fig 3.1). A typical experimental using this type of system is shown in Fig. 3.2.

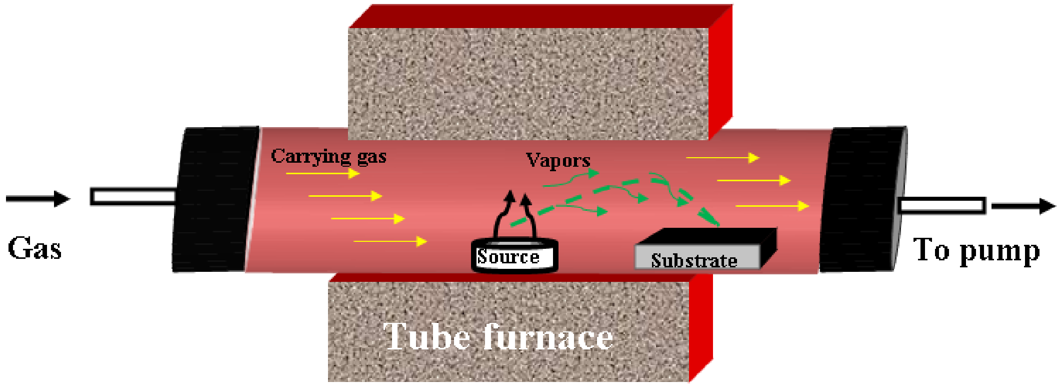

Figure 3.2. Schematic of the conventional thermal evaporate deposition system for the synthesis of 1D nanostructures.

High purity oxide powder that was contained in alumina boat was loaded in the middle of the furnace, where the highest temperature region was located. The substrates for collecting the desired nanostructures were usually placed down-stream of the source material (Fig 3.2). Substrates could be silicon or another type of semiconductor wafer. Both ends of the tube were covered by stainless steel caps and sealed with O-rings. During the experiments, the system was first pumped down to around 130-800 Pa. Then, the furnace was turned on to heat the tube to the reaction temperature at a specific heating rate. An inert carrying gas, such as argon or nitrogen, or a mixture of these gases with oxygen was then introduced into the system at a constant flow rate to bring the pressure in the tube back to 800-2700 Pa (different pressures were required by different source materials and final deposited nanostructures). The reaction temperature and pressure were held for a certain period of time to vaporize the source material and achieve a reasonable amount of deposition.

Source materials could be vaporized under high temperature and low pressure condition. The vapor was then transferred by the carrying gas down to the cooler region, where the vapor gradually became supersaturated. Once it reached the substrate, the nucleation and growth of nanostructures occurred. The growth was terminated when the furnace was turned off. The system was then cooled down to room temperature with flowing inert gas (usually nitrogen).

In some cases, oxide powders, like ZnO (1975 °C), have high melting points; therefore, use of a catalyst in the source material can decrease the melting point of the source. Owing carbothermal effects, graphite can cause a decrease in the melting point of a source material, like ZnO. Therefore, graphite is usually added as a catalyst to ZnO powder to reduce the ZnO melting point for the thermal evaporation method. The reaction between ZnO and graphite at ~950 °C could be:

$$ZnO(s) + C(s) \rightarrow Zn(v) + CO(v) \quad (3\text{-}1)$$

$$CO(v) + ZnO(s) \rightarrow CO_2(v) + Zn(v) \qquad (3\text{-}2)$$

3.1.2. Modification of thermal evaporation set-up

In addition of the conventional set-up that was described in the previous section, in this section the set-up is modified by a simple method. The set-up is modified by using a double-tube system, in which the interior tube is a one-ended tube (Fig. 3.3). Such a system makes the vapor environment regionally balanced and highly saturated, which is a key factor in the vertical growth of ZnO nanowires arrays. In fact, the double-tube system contains a quartz tube vacuum chamber 100 cm long and 5 cm in diameter. A smaller one-ended quartz tube, 50 cm long and 2 cm in diameter, which contained the precursor materials and substrate, was placed within the vacuum chamber. The precursor material of ZnO was placed at the closed end of the smaller quartz tube. Substrates locate downstream from the source material as shown in Fig. 3.3.

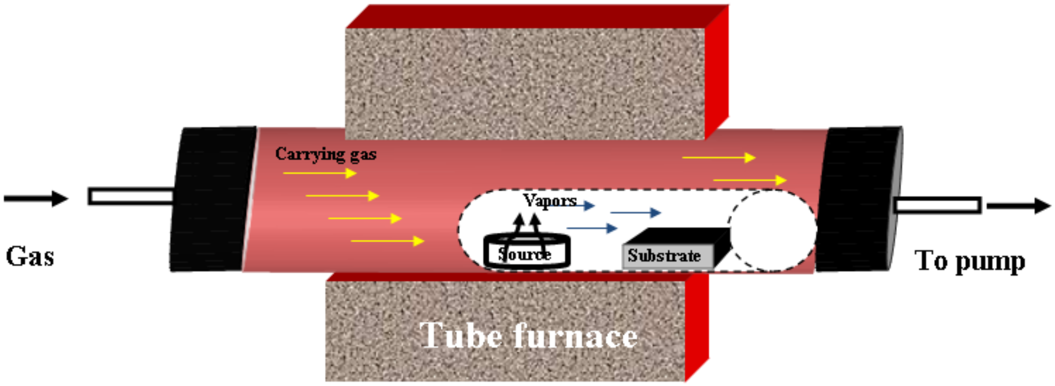

Figure. 3.3. Schematic of the modified set-up used for the growth of ZnO nanowires.

It is known that diffusion will occur even if the total pressure is uniform, as long as there is a spatial difference in the chemical potential, which is normally represented by differences in concentration or partial pressure, of the compounds of a gas mixture

(Kittel, 1969). The fundamental equation used to describe one-dimensional diffusion of a gas is Fick's first law. According to Fick's law, the diffusion flux is:

$$J= -D(dN/dx) \quad (3.3)$$

where J is the net flux of vapors (per unit area per unit time), D is the diffusion constant, and (dN/dx) is the concentration gradients of the vapors along the propagation direction (x) (Kittel, 1986). This means that the diffusion will always propagate toward the region with a lower concentration.

3.2. Epitaxial growth of nanostructures

Epitaxy is defined as the ordered growth of one crystalline material on another. This means that the growth process of the crystal will be affected by substrate properties. Crystal growth potential, whether epitaxial or not, can be determined by thermodynamics. A necessary condition for crystal growth is that there exists a chemical potential difference between the precursor materials and the material to be grown. This potential difference between vapor-phase materials and substrate can be determined by the flowing formula (Givargizov, 1975):

$$\Delta\mu = \mu_v - \mu_s = RT \ln (p/p_0) \quad (3\text{-}4)$$

where μ_v and μ_s are the chemical potentials of the vapor and substrate, respectively. In addition, p and p_0 refer to the partial pressure of the component in the gas phase and to the equilibrium partial pressure of that component over the crystalline material at the given growth conditions, respectively. Of course, this relation refers only to a one-component system; a binary system, including ZnO, is necessarily more complicated.

The thermal evaporation process is basically a physical vapor deposition process (PVD). It has been successfully used for the epitaxial synthesis of a variety of oxide and non-oxide nanobelts and nanowires. In this type of method, depending on whether a metal catalyst is used or not, the growth process is named vapor-liquid-solid (VLS) or vapor-solid (VS). In the VLS method, metals such as gold, tin, copper, silver, and nickel are usually used as catalysts.

3.2.1. Vapor-Liquid-Solid (VLS) method

Wagner and Ellis (1964) discovered the controlled catalytic growth of whiskers and, more recently, nanowires. They found that Si whiskers could be grown by heating a Si substrate that is covered with Au particles in a mixture of $SiCl_4$ and H_2, where the diameters of these structures are determined by the size of the Au particles. Wagner and Ellis named the VLS mechanism for the three phases that are involved: the vapor (V) phase precursor; the liquid (L) catalyst droplet; and the solid (S) crystalline product (Fig. 4.4). The main characteristics of VLS growth are that the nanowires have a metal or alloy droplet on their tips and that these droplets control their diameters and growth orientation.

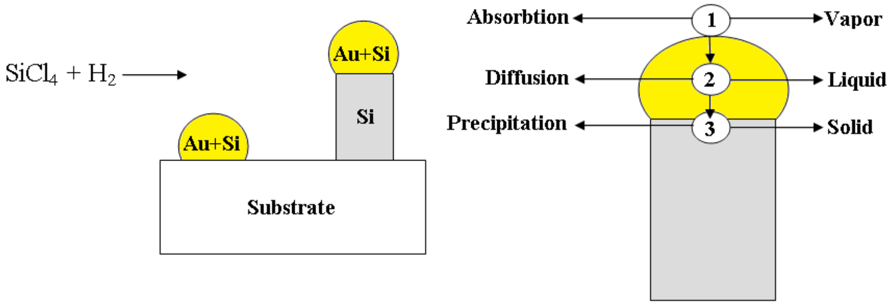

Figure 3.4. Schematic illustration of the growth mechanism of Si nanowires.

This method has also been used to grow ZnO nanowires. However, in contrast to elemental nanowires (e.g., Si), the growth process for oxide nanowires (e.g., ZnO) in this method is not very well understood at this time, due to the presence of oxidizing species (Yang *et al.*, 2002). In this thesis, the VLS method was usually used to grow

ZnO nanowires. A thin film of gold (10-30 nm thickness) was sputtered on the Si substrate using sputter coating process.

The sputter coater, model SPI, is shown in Fig. 3.5. Sputtering was performed by remote generation of high density plasma. The plasma was generated in a side chamber that opened into the main process chamber, which contained the target (Fig 3.5 (c)) and the substrate to be coated (Fig. 3.5 (b)). Generally, a gold film with thickness of 10-30 nanometers was used for our investigations. An experimentally determined thickness can be calculated from the following formula:

$$d=KIVt \qquad (3\text{-}5)$$

where d is the thickness of the gold in nanometers.

Figure 3.5. Sputtering system (model SPI) that was used in our lab for producing a gold coating on Si wafers.

K is an experimentally determined constant that depends on the metal (gold, in this case) being sputtered and the gas (Ar, in this case) being used; it is based on a distance of approximately 5 cm between the target and the specimen. K was approximately 0.017 for the gold that was used in conjunction with argon gas. I is the plasma current, V is the voltage applied (1 kV), and t is the sputtering time in seconds. Therefore, for a typical sputtering of gold in Ar with a plasma of 18 mA for 120 s, the value of d was 36.7 nm, (i.e., approximately 0.3 nm/s). The sputtering rate also depended on the cleanliness of the sputtering system.

After carrying out the gold sputtering, Si wafers coated with gold were annealed in an annealing furnace at 700 °C for 30 min, resulting in the formation of gold islands on the Si substrate. Figure 3.6 shows field emission scanning electron microscopy (FESEM) and atomic force microscopy (AFM) images of the Au nanoislands that were formed by a rapid thermal annealing of Au film at 700° C for 30 min, which was coated on a Si substrate. The size of these islands was dependent on the gold thickness and sintering temperature.

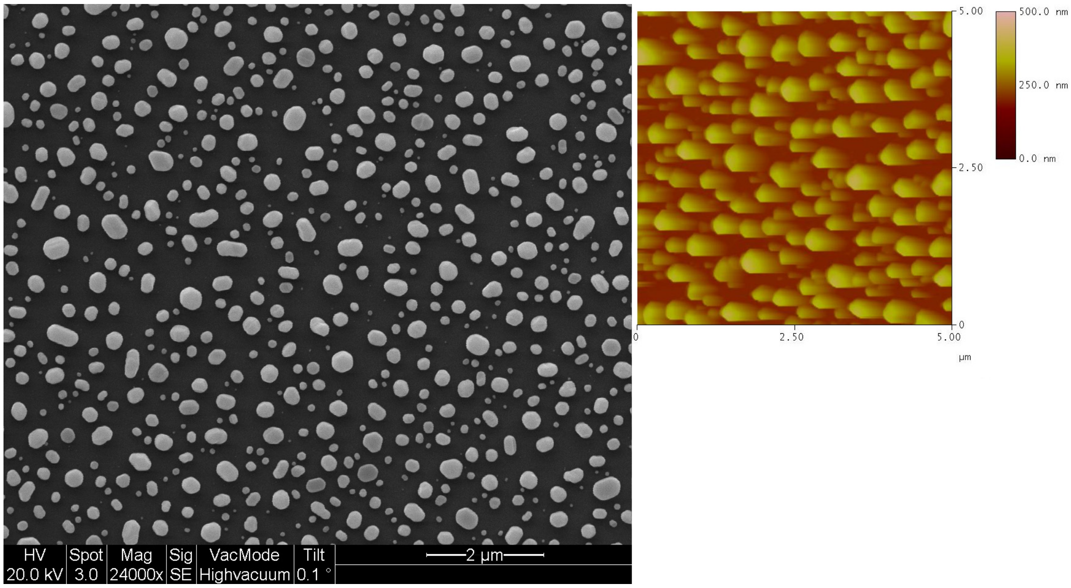

Figure 3.6. FESEM and AFM images of 30 s Au sputtered on a Si (111) substrate after 30 min of thermal annealing at 700° C.

These droplets became the preferred deposition sites for the formation of Zn_xO_y molecules from the vapor phase. After the liquid alloy was supersaturated with Zn_xO_y, the growth of ZnO nanowires took place by nucleation on the solid substrate/liquid droplet interface. Nanowires formed by the VLS process were characterized using the catalyst dots that were always located on their tips (Fig. 3.7).

Based on the carbothermal effect discussed in the previous section, as well as the growth of Si whiskers by the VLS method, the growth of ZnO nanowires are discussed here using the VLS mechanism. Zn atoms were transferred by the carrier gas to a lower temperature zone (downstream at ≈ approximately 400-700° C); therefore, Zn vapors transformed into the liquid phase in this zone. Owing to the higher sticking coefficient of Zn in the liquid phase, compared to the solid phase, Zn atoms have been shown to adsorb on the Au droplet surface (Park *et al.,* 2003).

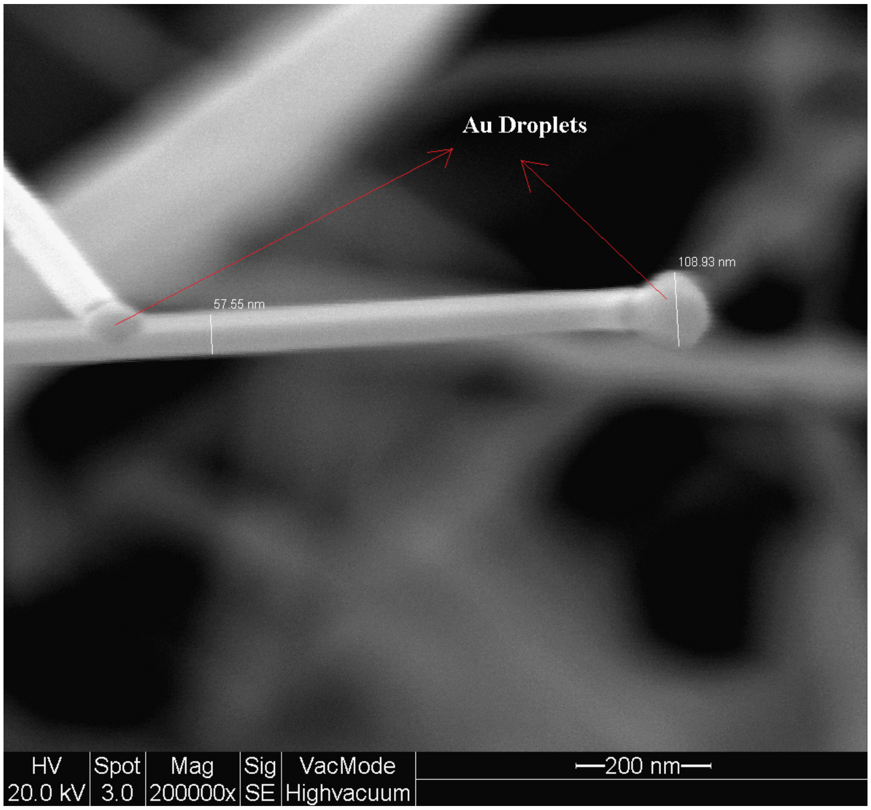

Figure 3.7. ZnO nanowires grown using the VLS method. Au droplets at the tips of these nanowires can be clearly observed.

Based on the Au–Zn phase diagram (Fig 3.8), it is expected that Zn precipitated from a liquid droplet, which can be formed in a Zn-rich region, via two possible reactions (Park *et al.*, 2003).

$\varepsilon(s) + L \leftrightarrow Zn(s)$ at 438° C (3-6)

$Zn(s) + L \leftrightarrow Zn(s)$ at 420- 438° C (3-7)

According to this phase diagram and reaction (3-6), a peritectic phase, formed from a mixed phase of the Au–Zn liquid alloy (L) and an intermediate solid phase (ε), was transformed into a solid Zn solution having a composition of 92.5 at % Zn. Reaction (3-7) occurred in the Zn-rich region (>92.5 at% Zn). In both cases, the solid solution of Zn transformed into two separate solid phases of ε and Zn during cooling to room temperature, as the solid solubility limit of Au in Zn is below 2 at % at room temperature.

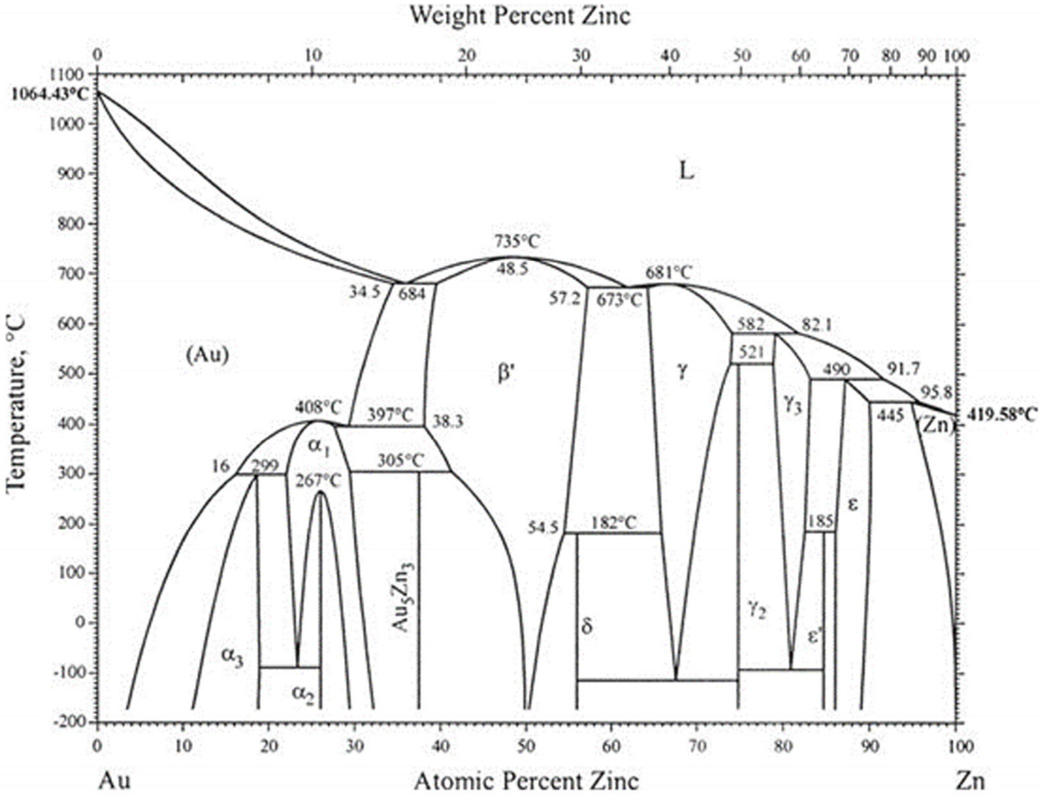

Figure 3.8. Au-Zn phase diagram. (http://resources.metapress.com/pdf-preview.axd?code=t747671152m4643k&size=largest).

The intermediate solid solution ε phase, which is stable below 490° C, had a composition ranging from 84 to 89 at % Zn. Using Energy-Dispersive X-ray (EDX) analysis, we found that the nanocluster at the tip of the nanowire only contained Zn and Au, and the composition of the nanocluster was measured as 88 at % Zn, which is within the detection limit of the measurement. In this regard, the Zn, which precipitated from the of ε + L or Zn + L phases; was considered to acts as a nucleation site for ZnO. As a result, ZnO nanowires grew via the VLS mechanism.

Figure 3.9 shows the VLS growth mechanism of ZnO nanowires, schematically. According to Low Energy Ion Scattering (LEIS) measurements, CO, CO_2, and O_2 cannot adsorb onto Au clusters (Zhang *et al.*, 1997). Bombarding a Zn-Au alloyed droplet with Zn atoms (Fig 3.9) results in a supersaturated, alloyed droplet and promote the formation of Zn islands at the substrate-droplet interface.

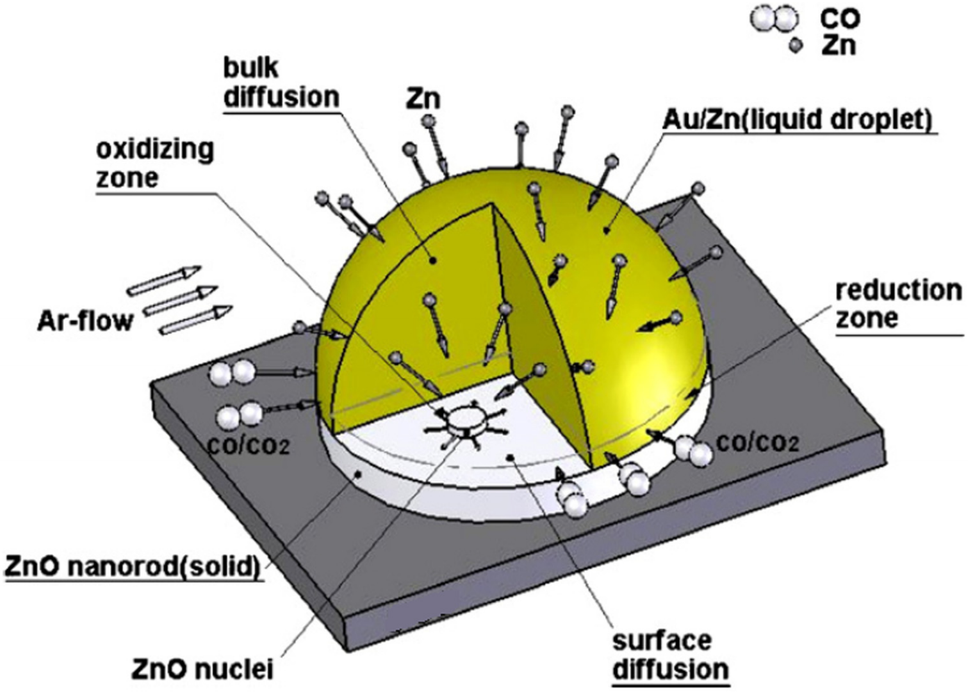

Figure 3.9. Schematic of ZnO nanowire formation by the VLS process (Hejazi *et al.*, 2008).

In addition to Zn atoms, CO/CO_2 is also transferred downstream of the source material by the carrier gas. Therefore, reaction between Zn and CO/CO_2 at droplet/substrate interface causes oxidized, condensed Zn islands by producing O^{2-} ions. In fact, a Zn-Au alloyed droplet can cause that each Zn atom to readily transform into the oxidizing species, resulting in the production of O^{2-} ions, owing to good electrical conductivity of the Zn-Au alloyed droplet (Hejazi *et al.*, 2008). The adsorptions-desorption process and ionization reactions involved in oxygen ion formation are shown in Fig 3.10 (a).

$Zn \rightarrow Zn^{2+} + 2e^-$ (3-8)

$CO_2(v) \rightarrow CO_2(ad) \rightarrow CO(ad) + O(ad)$ (3-9)

$CO(ad) + O(ad) + e^- \rightarrow O^-(chem.) + C(ad)$ (3-10)

$O^-(chem.) + e^- \rightarrow O^{2-}$ (3-11)

$Zn^{2+} + O^{2-} \rightarrow ZnO$ (nuclei) (3-12)

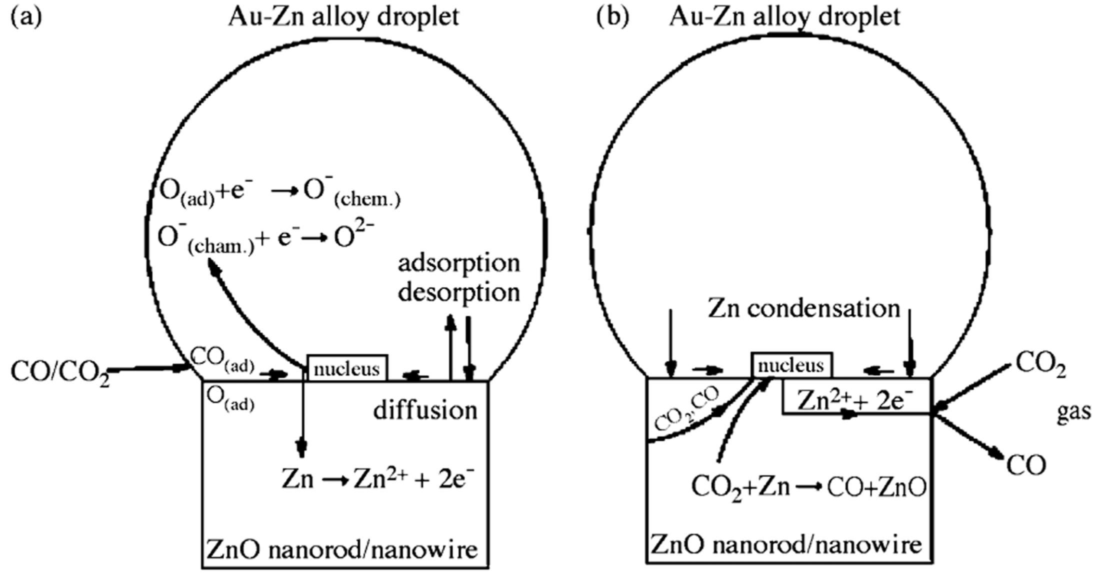

Figure 3.10. A model of ZnO nanowires growth by the VLS method: (a) schematic of the oxidation of Zn islands and nucleation of ZnO at the liquid-solid interface and (b) oxidation of a Zn island through nanorods (Hejazi *et al.*, 2008).

The droplet actually plays two roles: as an electrolyte for the diffusion of ions and as an electrical circuit for the passage of electrons. In addition, side-walls of the nanowires can be another source for the oxidation of Zn islands, as shown in Fig 3.10 (b) (Nagashima *et al.*, 2008).

3.2.2. Vapor-Solid (VS) method

Another common method to grow oxide nanostructures is the Vapor-Solid (VS) method. This method does not use any hetero-metals as catalysts. Of course, no theoretical techniques have been found for the growth of 1D nanostructure using the VS method. Some researchers believe that, in this method, Zn can play the role of a self-catalyst. In this method, Zn vapors can be generated via the carbothermal process in the high temperature region of a tube furnace. Then, the Zn vapor can be transported by carrier gas flow, or diffused, due to a temperature gradient, to a low temperature region in the furnace, where the Zn vapors are partly oxidized back to ZnO or ZnO_x species. Therefore, the Zn vapors will condense on the substrate to form liquid droplets. These droplets are preferred sites for the absorption of ZnO or ZnO_x vapor species. This means that Zn/ZnO or Zn/ZnO_x liquid droplets, like gold, will be formed and that ZnO nanowires or nanobelts will grow from the supersaturated liquid droplets. Yao *et al.*(2002) have observed this process with ZnO in the early stage of ZnO nanowires growth.

3.2.3. Different morphologies of 1D ZnO nanostructures

The crystalline nanowires are usually not cylindrical in morphology, but have a faceted shape that consists of certain low-index crystallographic planes. It is understood that the formation of wire-like nanostructures might be controlled by kinetics during crystal growth (Dai *et al.*, 2003). In this work, the likely 2D nucleation on the surface of a wire was established to be:

$$P_N = B \exp((-\pi\sigma^2)/(k^2 T \ln \alpha)) \qquad (3\text{-}13)$$

where P_N is the nucleation probability, B is a constant, σ is the surface energy of the solid wire, k is the Boltzmann constant, T is the absolute temperature, and α is the supersaturation ratio determined by p/p_0 (usually $\alpha > 1$), in which p is the actual vapor pressure, and p_0 is the equilibrium vapor pressure corresponding to temperature T (Dai *et al.*, 2003). The crystal planes in these structures are associated with surface energy, as a crystal plane having a lower index has a lower surface energy. According to Equation (3-13), a surface with lower energy causes a larger 2D nucleation probability. In addition, an atom adsorbed on low-surface energy has a weak binding energy and a high probability of desorption. These two factors are responsible for the formation of the low-index crystal planes that enclosing the nanostructure. In fact, supersaturation and temperature are the two main parameters that can be controlled by processing conditions. Therefore, a larger supersaturation ratio and higher temperature can be utilized to facilitate 2D nucleation, resulting in the formation of a sheet-like morphology. On the other hand, a smaller supersaturation ratio and lower temperature result in the growth of a wire-like morphology.

Based on the above explanation, in the case of ZnO, three types of fast growth direction can be: $<2\bar{1}\bar{1}0>$ ($\pm[2\bar{1}\bar{1}0]$, $\pm[\bar{1}2\bar{1}0]$, $\pm[\bar{1}\bar{1}20]$); $<0\bar{1}\bar{1}0>$ ($\pm[01\bar{1}0]$, $\pm[10\bar{1}0]$, $\pm[1\bar{1}00]$); and $\pm[0001]$.

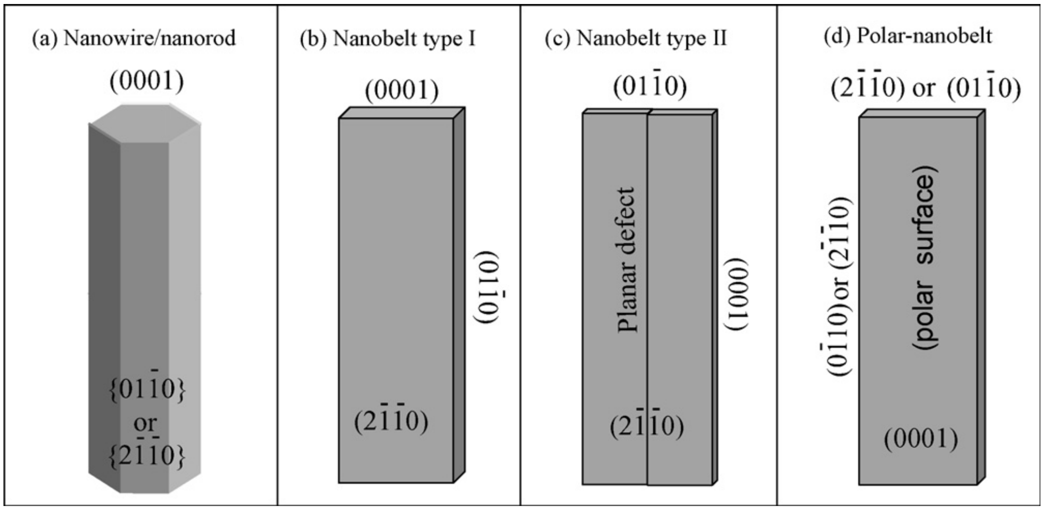

Figure 3.11. Typical growth morphologies of 1D ZnO nanostructures and the corresponding facets (Wang, Z.L 2004).

Therefore, ZnO can grow along directions that tend to maximize the areas of the $\{2\bar{1}\bar{1}0\}$ and $\{01\bar{1}0\}$ facets due to their lower energy (Fig. 3.11). Figure 3.11 (d) shows the polar surfaces of ZnO, which have been discussed in the previous chapter.

Figure 3.12 (a) shows an FESEM image of ZnO nanowires that were grown using VS method in a horizontal furnace. The inset in this figure shows a high-magnification FESEM image of a single nanowire that has a hexagonal face on its tip. No impurities, such as metal catalysts, were detected at its tip.

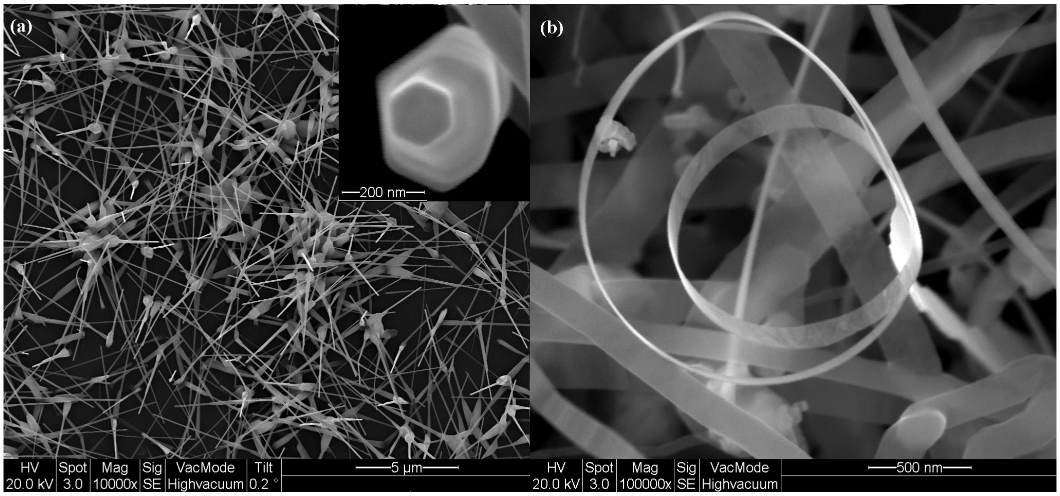

Figure 3.12. (a) ZnO nanostructures that were grown using the VS method: (a) ZnO nanowires (b) ZnO nanobelts and dual-nanorings.

Figure 3.12 (b) shows an FESEM image of ZnO nanobelts, which were also grown using the VS method in a horizontal furnace. In addition, this image shows a dual-nanoring that grew between the nanobelts.

3.3. Instrumentation

In this thesis, the morphological, structural, and optical properties of the samples were characterized using various techniques. These included field emission scanning electron microscopy (FESEM; Quanta 200F), transmission electron microscopy (TEM), select area electron diffraction (TEM/SAED; Philips FEI-CM200), X-ray diffraction

(XRD; Siemens D5000), field emission Auger electron spectroscopy (AES; JAMP-9500F), room temperature photoluminescence (PL; Jobin Yvon Horiba HR 800 UV, He-Cd laser, 325 nm, 20 mW), and Raman spectroscopy (Jobin Yvon Horiba HR 800 UV, Ar ion laser, 514.5 nm, 20 mW). In addition, field emission experiments were carried out by the Field Emission Microscopy group, headed by Professor Dilip S. Joag, in the department of physics, Pune University, India. A discussion of these instruments will be carried out in the following sections.

3.3.1. Field Emission Scanning Electron Microscope (FESEM) and Energy Dispersive X-Ray (EDX)

Scanning Electron Microscopy (SEM) is one of the most versatile and well-known analytical techniques. Compared to a conventional optical microscope, an electron microscope offers advantages that include high magnification, large depth of focus, and high resolution, as well as easy sample preparation and observation. In this technique, electrons generated from an electron gun enter the surface of a sample and generate many low energy secondary electrons. The intensity of these secondary electrons is governed by the surface topography of the sample. An image of the sample surface is therefore constructed by measuring secondary electron intensity as a function of the position of the scanning primary electron beam. In addition to secondary electrons imaging, backscattered electron imaging, and Energy Dispersive X-Ray (EDX) analysis are also useful tools that are widely used for chemical analysis. The intensity of backscattered electrons generated by electron bombardment can be correlated to the atomic number of the element within the sampling volume. Hence, qualitative elemental information can be determined. The characteristic X-rays emitted from the sample serve as fingerprints and give elemental information for the samples, including semi-quantitative and quantitative information, as well as the line profiling and spatial distribution of elements (elemental/chemical mapping). SEM with X-ray analysis is an efficient, inexpensive, and non-destructive method for carrying out surface analyses. In our microscopy lab, a state-of-the-art, high resolution FEI Quanta 200F field emission scanning electron microscope (FESEM) with an EDX system (INCA Energy 400) from OXFORD is available (Fig. 3.13).

Figure 3.13. A photograph of the FEI Quanta 200F FESEM with EDX set-up.

This is a high performance instrument designed for analytical applications and is controlled by a 32 bit computer system using Microsoft Windows 2000 as the operating system. Figure. 3.13 shows a photograph of this microscope in our lab.

3.3.2. Transmission Electron Microscope (TEM) and Select Area Electron Diffraction (SAED)

Transmission electron microscope (TEM) is a microscopy technique whereby a beam of electrons is focused onto an ultra thin specimen and transmitted through it, interacting with the specimen as it passes through. As a result of this interaction, an image is formed. The image is magnified and focused onto an imaging device, such as a layer of photographic film or a fluorescent screen, or is detected using a sensor (e.g., CCD camera). The magnified transmitted signal can be observed through direct electron imaging or electron diffraction. Electron diffraction patterns are applied to determine the crystallographic structure of the materials. As a result, the TEM image on the screen is a series of spots. In selected area electron diffraction (SAED), each spot corresponding to a satisfied diffraction condition of the crystal structure of the sample. If the sample is tilted, the same crystal will stay under illumination, but different diffraction conditions will be activated, causing different diffraction spots to appear or disappear. SAED is referred to as "selected" because the user is able to easily choose a selected part of the sample to obtain the diffraction pattern. In contrast with SEM, TEM analysis of a thin film sample is a destructive technique. In our lab, we used a Philips CM200 as TEM studies. This microscope is shown in Fig 3.14.

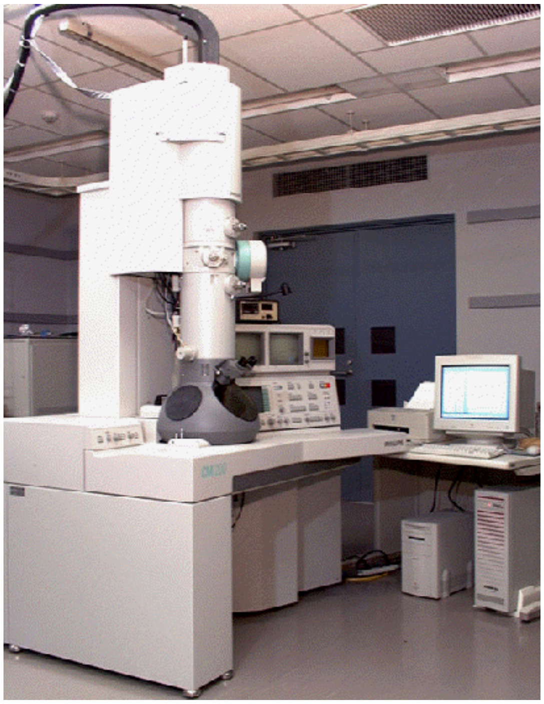

Figure.3.14 A photograph of the TEM microscope unit (Philips CM200).

In fact, a long process is necessary to prepare a thin film sample. In our lab, the sample is polished mechanically until it is about 10 μm thick, then translated to an ion-miller (Gatan PIPS) for further thinning with an ion beam (6kV, Ar gas) from the back of the sample surface. After a few minutes, the ion beam remove the substrate (Si) at the sample edge, leaving only a surface of ZnO behind. At this time the sample can be analyzed with TEM for inspection.

3.3.3. X-Ray Diffraction (XRD)

One of the most important non-destructive tools for the analysis of all kinds of crystalline matters is X-ray diffractometer. Two important characteristics can be obtained using X-ray diffraction (XRD) pattern produced by this technique. These include a fingerprint characterization of the crystalline materials and a determination of their structure. The fundamental of XRD analyses are based on Bragg's law. When X-rays of wavelength λ are incident at an angle θ on a crystal lattice, a portion of these beams will be scattered in all directions. The necessary and sufficient condition for constructive interference is known as Bragg's law. According to this law, scattered waves originating from each atom will be in phase with each another. Figure 3.15 shows the geometric requirements for this condition. Bragg's law is follows:

$$n\lambda = 2d_{hkl} \sin\theta \tag{3-14}$$

All characteristics of this formula are introduced in Fig. 3.15. d_{hkl} as the interplanar spacing as a function of the Miller indices (h, k, and l) as well as the lattice parameters.

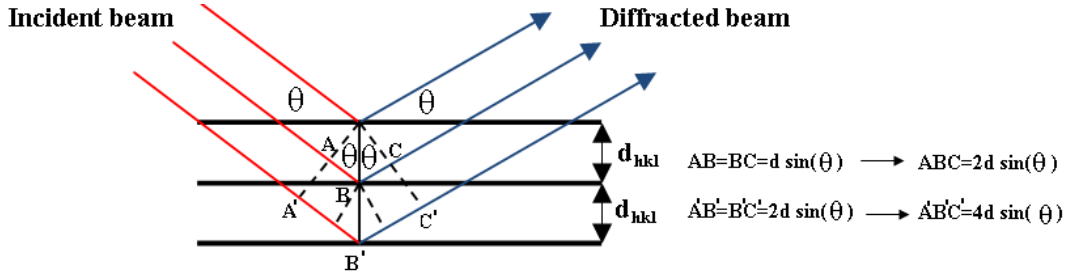

Figure. 3.15. Schematic of the diffraction of an X-rays beam by parallel atomic planes in a crystalline material.

For example, for ZnO with a hexagonal structure, d_{hkl} is given by the following relation (Cullity, 1956):

$$d_{hkl} = \left[\frac{3}{4\left\{ \frac{h^2 + k^2 + hk}{a^2} + \frac{3l^2}{4c^2} \right\}} \right]^{1/2} \qquad (3\text{-}15)$$

The basic features of a typical XRD experiment, as well as our XRD set-up, are shown in Fig. 3.16. We used a Siemens D5000 XRD unit, with an X-ray source having wavelengths of $K_\alpha = 1.5406$ A°. Usually, diffraction experiments were applied at a fixed wavelength; therefore, measurement of the diffraction angles enables calculation of the associated d_{hkl} and then the lattice constants.

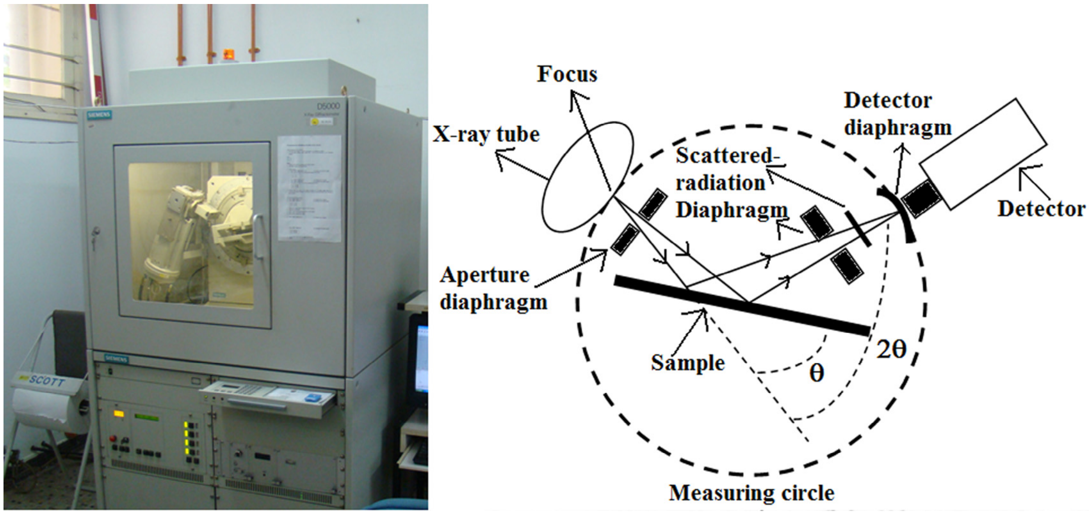

Figure. 3.16. Basic features of a typical XRD experiment as well as the Siemens D5000 set-up.

3.3.4. Auger electron spectroscopy (AES)

Auger electron spectroscopy (AES) determines the elemental composition of the few outermost atomic layers of materials. AES is an established analytical technique for the analysis of solid surfaces. It has recently attracted particular attention because of its ability to perform elemental analyses on sub-micron areas, and through the improved accuracy of these examinations. In this technique, a focused beam of electrons with energies from 3 to 30 keV bombards the surface of a specimen. The core-level electrons are ejected from approximately the first 1 μm of a sample, resulting in a vacancy in the core-level. As the atom relaxes, an outer-level electron fills the core vacancy and releases excess energy. This, in turn, ejects an outer electron, known as an Auger electron. This process is illustrated in Fig. 3.17.

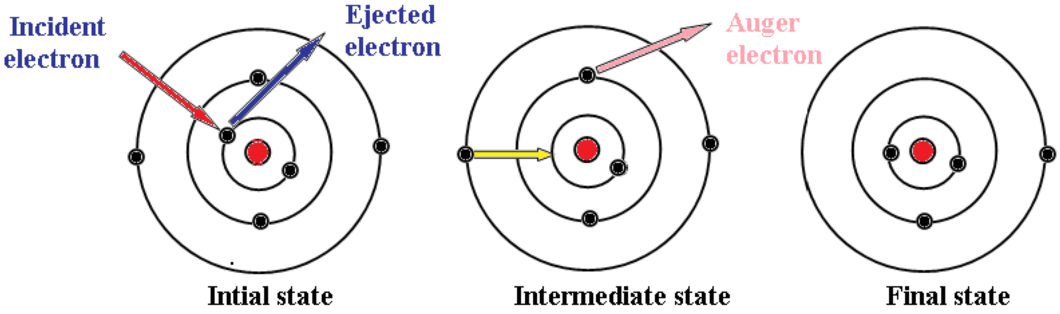

Figure. 3.17. Schematic of a generated Auger electron emission.

The kinetic energy of Auger electrons is characteristic of each element, with the exception of hydrogen and helium. Therefore, by measuring the energies of Auger electrons, the near-surface composition of a specimen can be identified. In addition, if the system is equipped with an ion gun to sputter away material, AES can provide a compositional depth profile from relative intensities of the elements present. In our lab, a field emission Auger electron spectroscopy unit (AES, JEOL JAMP-9500F) is available (Fig. 3.18).

The JAMP-9500F Auger microprobe essentially consists of an ultra-high-vacuum (UHV) system with an air-lock sample exchanging chamber, a primary electron irradiation system for sample excitation, a cylindrical mirror electron energy analyzer, an ion sputtering gun and a secondary electron detector for SEM image observation. The analyzing chamber is evacuated down to 10^{-8} Pa by a sputter ion pump and titanium sublimation pump. The air-lock chamber is evacuated by a turbo-molecular pump. Conventionally, AES has involved the study of Auger spectra obtained by differentiating the observed electron energy distribution [dN(E)/dE], which consists of Auger electron peaks superimposed on the more intense secondary electron spectrum. Even though an unambiguous interpretation of Auger spectra is facilitated by the use of dN(E)/dE spectra, a large amount of useful information available in the original N(E) spectra is lost in differentiation. Direct observation of the undifferentiated N(E) spectrum has been discovered to facilitate an Auger analysis that provides both decreased sensitivity toward to surface topology and more comprehensive information about surface properties [Handbook of Auger Electron Spectroscopy (JEOL)]. For this reason, we also used this method for the Auger study of our samples.

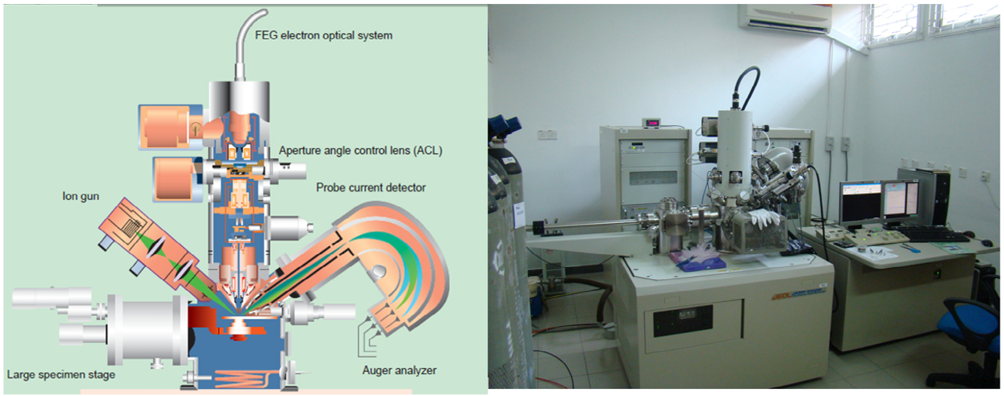

Figure. 3.18. AES, JAMP-9500F set-up in our lab as well as schematic of all process in Auger spectrometer.

3.3.5. Photoluminescence and Raman spectrocopies

Figure 3.19 shows a phtograph of PL and Raman spectrometers (Jobin Yvon Horiba HR 800 UV) at our lab, which is used for PL and Raman studies in this thesis. PL and Raman studies in this thesis were conducted at room temperature for all of ZnO nanostructures. The source of these spectrometers are a He-Cd laser using excitation with 325 nm emission at 20 mW power level (for PL) and an Ar ion laser with a wavelength of 514.5nm emission (for Raman).

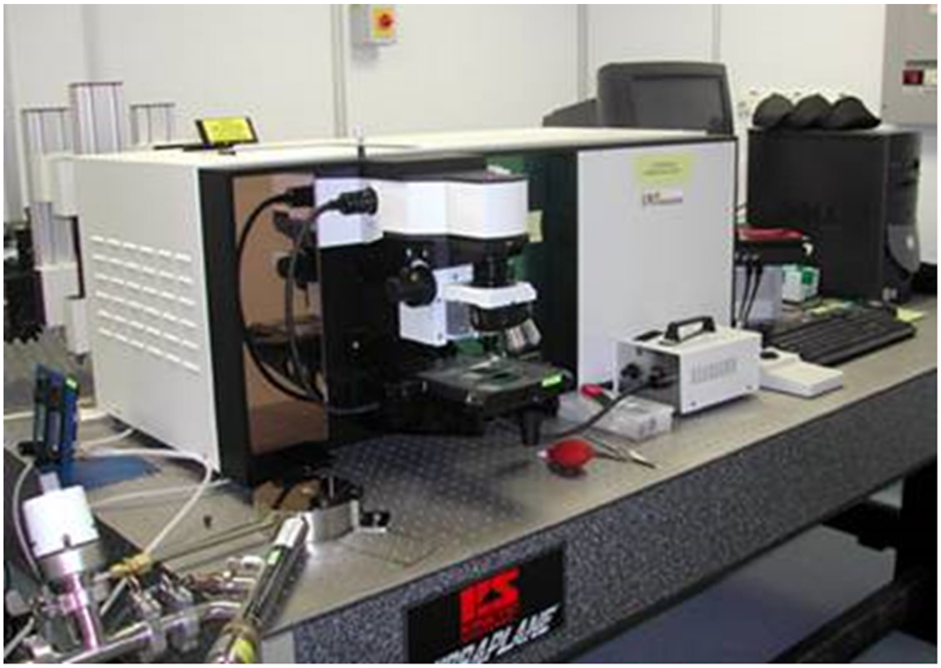

Figure 3.19. PL and Raman spectrometers set-up, model: Jobin Yvon Horiba HR 800 UV.

3.3.6. Field emission measurements

In close proximity (C-P) or parallel plate diode configurations, the cathode is in the form of a thin film, which is held in front of an anode (a metal sheet or a semitransparent phosphor screen). The conducting anode screen is prepared by coating a cathodoluminescent phosphor onto a SnO_2 coated glass plate. The typical separation between cathode and anode in the C-P configuration varies from 50 µm to a few mm. Either the emitter cathode or the anode screen is attached to a linear motion drive, to facilitate variation in the cathode-anode separation. The field emission study of thin film cathodes or nanostructure arrays is carried out in the C-P configuration.

In the C-P configuration, the electric field, generally termed as the average electric field is given by $E = \frac{V}{d}$, where d is the separation between the cathode and anode and V is the voltage applied to the cathode. In the case of a thin film emitter consisting of anisotropic structures (e.g., nanowires, nanoneedles, naobelts), the local electric field at the apex of these structures is defined by (Jang *et al.*, 2005):

$$E_{local} = \frac{\beta V}{d} \tag{3-16}$$

where β is the field amplification factor or local field conversion factor. Usually, for a single nanowire or a nanoneedle, the field enhancement factor β is defined as

$$\beta = \frac{h}{r} \tag{3-17}$$

where h is length of the wire and r is the wire diameter. Recently, according to the Filip model (Filip *et al.*, 2001) the local electric field at the apex of the emitter is given as:

$$E_{\mathrm{local}} = s\frac{V}{r} + (1-s)\frac{V}{d} \tag{3-18}$$

where r is the radius of the emitter and s is a parameter describing the degree of the screening effect ($s = 0$, for densely arranged emitters, and 1, for a single emitter).

A schematic diagram of the C-P configuration and a photograph of the all metal FEM system (containing the C-P arrangement) are shown in Fig. 3.20.

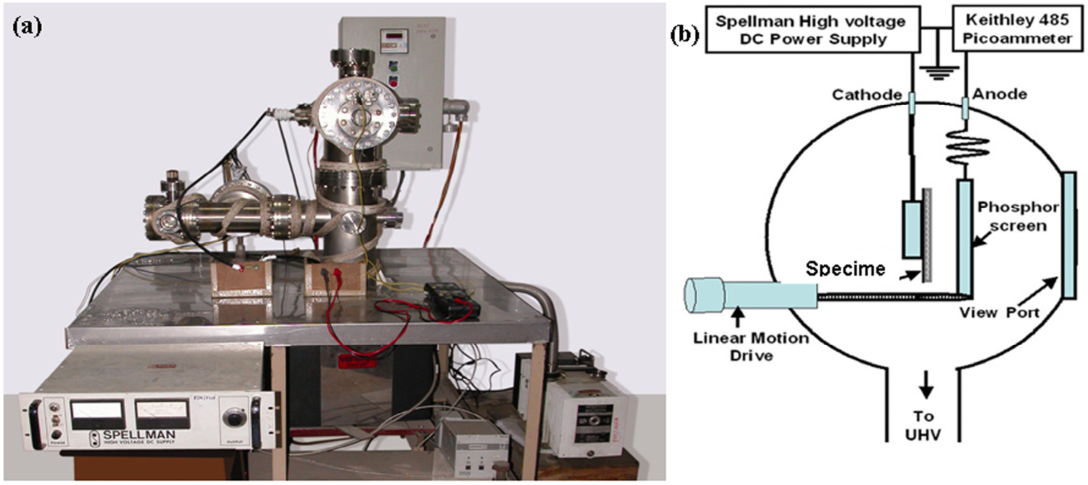

Figure 3.20. (a) Instrument used for field electron emission studies, (b) Schematic diagram of the planar diode configuration assembly.

The as-synthesized and annealed thin film specimens on the substrate were used as field emitter cathodes in a planar diode configuration. The sample was mounted onto a stainless-steel stub (ϕ ~ 6 mm) using silver paste, for proper ohmic contact. A phosphor screen, which was used as the anode, was held parallel to the cathode, and was mounted on a linear motion drive. The linear motion drive facilitated variation in the cathode-anode separation. The cathode-anode assembly was introduced into a metal chamber, which was mounted in a UHV system.

For the field emission current-voltage (*I-V*) and current-time (*I-t*) measurements, the experimental setup consisted of a Spellman high voltage power supply (± 40 kV), a Keithely 485 Picoammeter and the planar diode configuration assembly. After making proper electrical connections [as depicted in Fig. 3.20(b)], the voltage applied to the cathode (emitter, specimen) was increased very carefully and the resulting emission current was measured on the electrometer. The turn on voltage was usually defined as the value of the applied voltage required to draw an emission current of 1 nA. The *I-V* measurement dealt with recording the applied voltage and corresponding field emission current values, which could be span over a wide range (from 1 nA to several hundred μA). In general, the turn-on field value strongly depends upon the tip morphology, size, density, crystallinity, and alignment of the 1D nanostructures (Yang *et al.*, 2006).

Carefully, increasing the cathode voltage resulted in the observation of a field emission image on the screen. The photographs were recorded with a digital camera. At least three sets of measurements were taken to check the reproducibility of the experimental results. The current-versus-voltage (*I-V*) data were used to plot current density versus applied field curve and F-N plot. The nature of the F-N plot verified the quantum mechanical tunneling phenomenon of field electron emission. The slope of the F-N plot in the linear region was used to determine the value of the field enhancement factor (β). In each case, the emission current density (J) was obtained by dividing the emission current (I) value by the total area of the emitter surface (A; i.e., $J = I/A$).

The emission current stability is a decisive property for the application of the cathode in field emission based devices. The current stability is recorded for preset current values at a fixed voltage. For the field emission current stability (*I*-*t*) measurements, application of a fixed voltage to the cathode yielded an emission current that was set as the initial value. (several nA to several μA, as per the specimen), and the emission current values were recorded after an interval of 10 or more seconds. For long term stability measurements, values of the field emission currents were recorded for durations of more than three hours. After taking the proper precautions, the *I*-*V* and I-t measurements were performed at a base pressure of 1×10^{-8} mbar with the cathode at room temperature.